Langmuir

ARTICLE

pubs.acs.org/Langmuir

Influence of Electrostatic and Chemical Heterogeneity on the Electric-Field-Induced Destabilization of Thin Liquid Films

Arnab Atta, David G. Crawford, Charles R. Koch, and Subir Bhattacharjee*

Department of Mechanical Engineering, University of Alberta, Edmonton, Alberta, Canada

ABSTRACT: A numerical model for thin liquid film (<100 nm) drainage in the presence of an external electric field is developed. Long-wave theory is applied to approximate and simplify the governing equations. A spatiotemporal film morphology evolution equation thus obtained is then solved using a combination of finite difference to resolve the spatial dimensions and an adaptive time step ODE solver for the temporal propagation. The effect of fluid properties, namely, viscosity and surface tension, on the film drainage time is observed for a homogeneous electric field, which leads to random dewetting spots. Electrically heterogeneous fields, achieved by modeling electrodes with various periodic patterns, are explored to identify their effect on the drainage time and behavior. Finally, the chemical heterogeneity of the substrate is coupled with the periodic electric heterogeneity to understand the implications of combined heterogeneity. It is observed that the introduction of any heterogeneity results in faster drainage of the film when compared to that of the homogeneous field. In all cases, the thin film is drained, leaving submicrometer-scale structures at the interface. Well-controlled surface patterns are found on the application of periodic heterogeneity. This study effectively demonstrates the immense potential of electrically induced thin film drainage as a means for faster de-emulsification and for the creation of ordered submicrometer-scale surface patterns on soft materials.

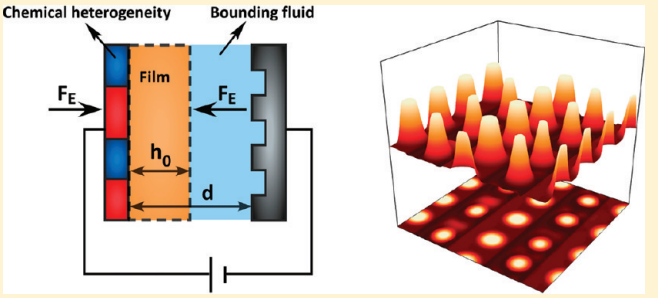

INTRODUCTION

Thin liquid films are frequently encountered in various scientific and technological applications, including de-emulsification, coating, biological membranes, optoelectronic devices, sensors, biochips, and so forth.[1−4] For example, in emulsions that consist of multiple immiscible liquid phases, a thin film of a continuous phase separates two droplets of the dispersed phase before their coalescence. Generally, this droplet−droplet coalescence is preceded by the process of thinning/drainage and finally the rupture of the intervening thin liquid film.[5] Consequently, the emulsion stability depends on the stability of such thin liquid films.[6−8] Unraveling the properties and drainage behavior of these thin films can provide significant insights into the surface forces that are responsible for the macroscopic stability of the emulsions. The rupture of thin films can take place through a diverse range of drainage dynamics when subjected to mechanical, thermal, chemical, or electrical perturbations.[5,9−25] It has been pointed out that the phenomena responsible for thin film drainage are different from flow in typical bulk fluids and pose unique challenges to its mathematical description.[26] Moreover, a single thin liquid film itself has a wide range of application in several biological, physical, and engineering systems.[27] Because of attractive micro- and nanopatterns originating from the growth of their surface instabilities, thin films have also received extensive attention over the last two decades as a means of developing novel nanostructured materials.[28−39]

With the recent advances in lithographic methods, novel micro- and nanopattern creation at the interface of soft matter (for example, thin liquid films) has become a viable approach to the rapid, and economic fabrication of nanostructures.[27] Researchers have employed electrohydrodynamic (EHD) lithography in which surface patterns are induced by an external electric field as a promising alternative over several other fabrication techniques (e.g., nanoimprinting, soft lithography, self-assembly, etc.).[27,40−43] In this context, it is noteworthy that improved control and structured patterning can be easily attained by introducing substrate physicochemical heterogeneities and/or electric field heterogeneity.[3,44] Another significant advantage of using EHD is the accomplishment of control over the size scale of the surface patterns.[45−47] Numerous experimental studies on EHD have described the morphological evolution of single and/or multilayered polymeric,[17−19,40,41,45−48] metallic alkoxide,[20] and photocurable[49,50] materials to fabricate novel surfaces for various potential applications. These studies have reported the formation of pillar structures that closely depend on the fractional filling of the capacitor gap.[19] The dynamic adjustment of the gap during morphological evolution helped to achieve stretched pillars with an increased aspect ratio.[50] Experiments also indicate that a systematic reduction in the wavelength of the surface instabilities

Received: July 18, 2011
Revised: August 31, 2011
Published: September 02, 2011

dx.doi.org/10.1021/la202759j | *Langmuir* 2011, 27, 12472–12485

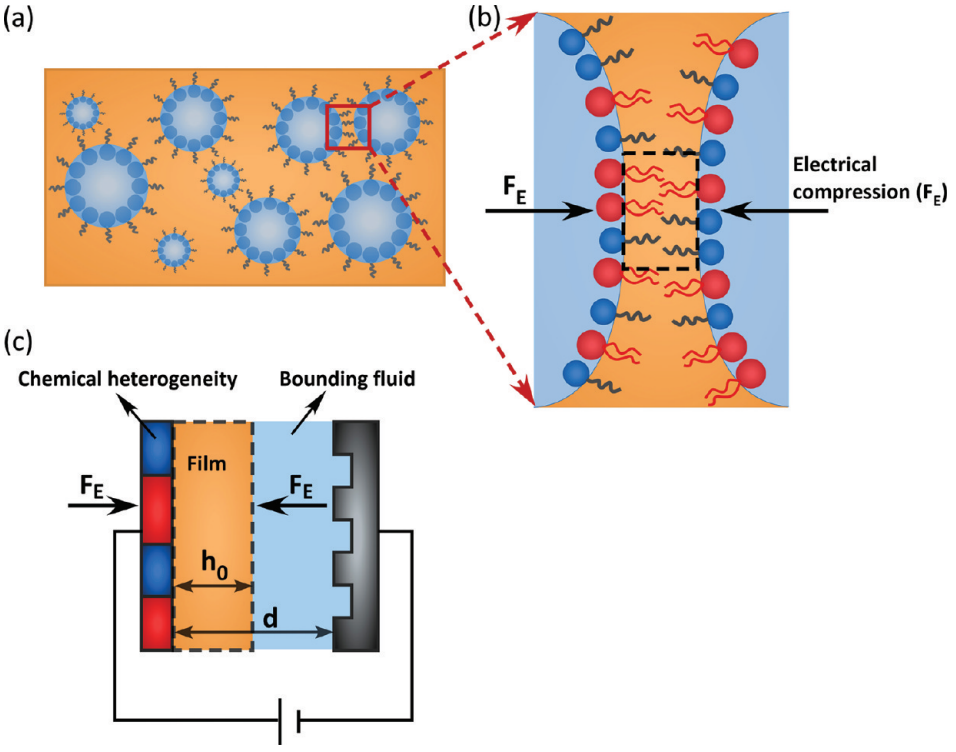

Figure 1. (a) Schematic of thin film formation in between two adjacent droplets approaching each other in an emulsion for coalescence in the presence of surface-active agents. (b) Enlarged view of the thin liquid film subjected to an electrical compression with force F_E in the presence of different chemical additives. The red and blue surfactants impart chemical and electrical heterogeneity to the interfaces. (c) Conceptualized schematic to represent the combined effect of chemical and electrical heterogeneity on single thin film drainage.

can be anticipated by the addition of conductive nanoparticles in polymer/nanoparticle nanocomposite thin films as a result of the increased dielectric constant of the films.[48]

Several theoretical studies have been carried out to elucidate the patterning process as well as to identify the conditions for the formation of ordered patterns on single and/or multilayer thin films when subjected to EHD surroundings.[3,51−62] Despite considerable theoretical attention dedicated to understand the pattern formation in thin films (polymeric films in particular) by the application of electric fields, most of these studies have primarily addressed the relationship between the pertinent length scales and the range of interactions that determine the final morphology of the film after drainage. It has also been shown that developed surface patterns will continue to evolve over time and will ripen afterward,[47,53] unless such structures are "frozen" at a desired stage.

While assessing the stability of water-in-oil emulsion films, studies have reported that these emulsions are generally stable with their characteristic disjoining pressure[8,63] (Figure 1a). The disjoining pressure is the measure of excess pressure arising from the molecular interactions between two interfaces, and it is dependent on the film thickness.[63] In practice, chemical additives (predominantly surface-active agents) are used to lower this energy barrier by reducing the interfacial tension in order to accomplish faster de-emulsification.[64] Some recent experiments have demonstrated that the presence of an external electric field can lead to very rapid drainage of such free films compared to conventional pressure-based drainage[64−66](Figure 1b). Our early theoretical studies also investigated and supported this phenomenon by comparing the drainage times and final patterns to those obtained during solely pressure-based drainage.[67] During the compression of the liquid film in emulsions by the application of an electric potential, an interesting situation may arise if different additives and surfactants are mixed together in an emulsion. It can be observed from Figure 1b that different additives and surfactants will eventually introduce chemical heterogeneity at the interfaces. In the final stages of film thinning, when the thickness is reduced to about 100 nm, surface forces influence the rupture and drainage behavior.[5,68] In that scenario, even a homogeneously applied external force or field may effectively result in nonuniform or heterogeneous pressure gradients on those interfaces. Therefore, some understanding of the combined effects of the electric field and chemical heterogeneity of the interface on an isolated single thin film (<100 nm) becomes important.

In this article, we present a highly simplified model of these complex drainage phenomena as the schematic presented in Figure 1c. This figure depicts a system of a single liquid film resting on a solid substrate having chemical heterogeneity. The liquid film effectively represents the film-forming fluid within the dotted rectangle in Figure 1b and is essentially homogeneous. Both the chemical and electrical heterogeneity of the bounding fluids are manifested through the body forces experienced by the film. This chemical heterogeneity effect can also be combined with the effect of electric field heterogeneity by periodically patterning another substrate (the working electrode). Figure 1c represents an interesting surrogate for modeling film drainage from the perspective of rapid electrocoalescence in a chemically and electrically heterogeneous system. To facilitate thin film rupture (for faster de-emulsification) and achieve the desired

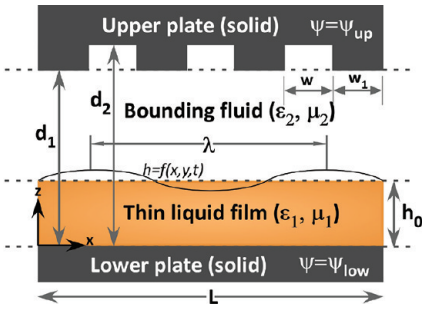

Figure 2. Schematic of the thin film system. For a homogeneously applied electric field, $d_1 = d_2 = 100$ nm. In cases of electrically heterogeneous systems, $d_1 = 100$ nm and $d_2 = 188$ nm.

structured surfaces (in cases of novel material synthesis), insights into the drainage behavior and estimation of the characteristic drainage time of such a single heterogeneous thin film system could be of considerable benefit.

The situation in Figure 1b, (i.e., trilayer drainage) has been addressed for van der Waals forces[69] as well as electrohydrodynamic forces[57] using linear stability analysis. None of these studies consider the chemical heterogeneity of the film. It is indeed difficult to consider heterogeneity on simultaneously deforming interfaces, which is the rationale for using our surrogate model as in Figure 1c. Chemical heterogeneity plays an important role in thin film instability for van der Waals-driven dewetting[24] and electric-field-induced pattern formation.[61] Srivastava et al.[61] studied the coupled influence of chemical and electrical heterogeneity by applying a spatial dielectric constant contrast for pattern formation in thin films. However, to the best of our knowledge, no previous study considers the effect of the chemically patterned variation of van der Waals interactions in conjunction with physically patterned electrodes to vary the electrical and chemical heterogeneity independently.

The present numerical work initially explores the thin liquid film drainage behavior under the influence of an externally applied electric field. Following this, we distinguish the effect of fluid properties, namely, surface tension and viscosity, on the drainage behavior. As interesting nanoscale surface patterning can be accomplished through the drainage of thin films, the spatiotemporal evolution of the film morphology is studied. To examine the effect of field heterogeneity on the film drainage time, periodic electrical heterogeneity was incorporated in the model by physically patterning the top electrode. To elucidate the influence of the periodicity of the electric field on the drainage behavior and final film morphologies, parametric studies on the electrical heterogeneity have been carried out. Finally, the chemical heterogeneity of the substrate has been integrated by the contrast into an effective Hamaker constant and has been coupled to the electrical heterogeneity to identify its importance in thin film drainage.

MATHEMATICAL MODELING

The geometrical parameters pertaining to the ultrathin liquid film system (<100 nm), confined between two periodically patterned electrodes, are schematically shown in Figure 2. It is evident that when such a thin film is perturbed, depending on the initial film thickness, the perturbations may be attenuated or may grow in a periodic manner, creating waves on the film.[70,71] In the latter case, the characteristic wavelengths (λ) of the disturbance are found to be significantly larger than the mean film thickness (h_0). This difference in the length scale between the film thickness and the waves that are formed on the film interface allows the simplification of the governing equations using the long-wave approximation.[26]

As shown in Figure 2, a thin liquid film having an initial film thickness of h_0 is enclosed between two electrodes with an interelectrode spacing of d. It is then perturbed by an infinitesimal disturbance, resulting in a film thickness of $h(x, y, t)$ in Cartesian coordinates (x, y) and time (t). This thin film is surrounded by a bounding fluid. The viscosity and permittivity of the fluids are designated by μ and ε, respectively, where subscript i indicates the fluid phase under consideration with $i = 1$ for the film and 2 for the bounding fluid. The applied voltages are marked as ψ_{up} for the upper electrode $(z = d)$ and ψ_{low} for the lower electrode $(z = 0)$. In this context, for a homogeneously applied electric field, it is apparent that $z = d = d_1 = d_2$. A periodically heterogeneous field can be produced by setting different values of d_1 and d_2 $(d_1 \neq d_2)$. A higher initial electric field will be experienced by the film interface in the segments with $d_1 < d_2$ having a width of w_1 in such a conformation. The width of lower-field-strength segment is designated by w.

Governing Equations. This thin film system is considered to be isothermal and Newtonian. It has been modeled using a continuum assumption, and the governing equations are defined by the set of Navier−Stokes (NS) and continuity equations. Fluid properties such as the density (ρ), viscosity (μ), surface tension (γ), and dielectric constant (ε) are assumed to be constant.

$$\rho_i\left[\frac{\partial \vec{u}_i}{\partial t} + (\vec{u}_i \cdot \nabla)\vec{u}_i\right] = -\nabla p_i + \nabla \cdot [\mu_i(\nabla \vec{u}_i + (\nabla \vec{u}_i)^T)] + \vec{f}_i \quad (1a)$$

$$\nabla \cdot (\vec{u}_i) = 0 \quad (1b)$$

where $\vec{f}_i (= -\nabla\phi_i)$ represents the body forces and ϕ_i is the conjoining/disjoining pressure.[26] At the upper and lower electrodes, no slip boundary conditions are applied.

$$\vec{u}_1 = 0 \text{ at } z = 0 \quad \vec{u}_2 = 0 \text{ at } z = d \quad (2)$$

At the interface, a continuity of velocity is assumed.

$$\vec{u}_1 = \vec{u}_2 \text{ at } z = h(x,y,t) \quad (3)$$

The interfacial velocity is related to the film thickness by the following kinematic condition.[71]

$$\omega = \frac{\partial h}{\partial t} + u\frac{\partial h}{\partial x} + v\frac{\partial h}{\partial y} \text{ at } z = h(x,y,t) \quad (4)$$

To simplify and solve the governing equations for this system, we assume (a) the fastest-growing disturbance is uniform in both the x and y directions; (b) the two fluids are modeled as immiscible with no interphase mass transfer across the fluid−fluid interface; (c) the film is sufficiently thick that the continuum assumption remains valid but sufficiently thin that the effect of gravity can be disregarded; (d) the viscosity ratio of the film to the bounding fluid is large $(\mu_1/\mu_2 \gg 1)$; and (e) inertial effects will be negligible because the considered fluid film is thin ($h_0 <$ 100 nm). These simplifications, along with the consideration of leading-order terms after applying the long-wave approximation[26] (i.e., $h_0/\lambda \ll 1$), yield the dimensionless spatiotemporal evolution

of the thin film height, $H(= h/h_0)$, which can be represented in the following dimensionless form

$$\frac{\partial H}{\partial T} + \frac{\partial}{\partial X}\left[H^3\frac{\partial \Psi}{\partial X}\right] + \frac{\partial}{\partial Y}\left[H^3\frac{\partial \Psi}{\partial Y}\right] = 0 \quad (5)$$

where

$$\Psi = \frac{\partial^2 H}{\partial X^2} + \frac{\partial^2 H}{\partial Y^2} - \Phi \quad (6)$$

in which Φ represents the overall scaled disjoining pressure acting on the film as a result of intermolecular interactions and the external electric field. The scaled spatial dimensions are given by $X = x/\lambda$, $Y = y/\lambda$, and $T = tu_0/\lambda$, where u_0 is the characteristic velocity. More detailed derivations of these equations can be found elsewhere.[26,67]

Disjoining Pressure. As the considered liquid film is very thin (<100 nm), the length scale of intermolecular interactions is comparable to the film thickness.[70,72] The strength and range of the intermolecular forces that are predominantly classified as the Lifshitz−van der Waals (LW), electrostatic, and polar interactions depend on the physical and chemical properties of the system.[72] The intermolecular force considered in this work consists of only the LW force. The conjoining/disjoining pressure in the film due to the LW forces can be written as[44,70]

$$\phi_{LW} = \frac{A_L}{6\pi h^3} \quad (7)$$

where A_L is the effective Hamaker constant for interactions between the upper (free) surface of the film and the lower solid surface through the fluid film. The above expression results in the divergence of the van der Waals energy as $h \rightarrow 0$. Another case of divergence can appear as a consequence of the top surface wetting during surface instability and morphological evolution. To ensure nondrying and nonwetting of lower and upper electrodes, respectively, a short-range repulsion similar to Born repulsive forces[73] has been included in this work. This inclusion helps in maintaining a minimum equilibrium liquid thickness (l_0) on the lower solid surface. It also removes the contact line singularity by preventing the wetting of the upper electrode.[3] The expressions for these repulsive forces at lower and upper electrodes are respectively[73]

$$\phi_{B_L} = -\frac{8B_L}{h^9} \quad (8)$$

$$\phi_{B_U} = \frac{8B_U}{(d-h)^9} \quad (9)$$

where the constants (B_L and B_U) are found by setting the conjoining/disjoining pressure equal to zero at the upper and lower surfaces:

$$B_L = \frac{\phi_{(z=l_0)} l_0^9}{8} \quad (10)$$

$$B_U = \frac{\phi_{(z=d-l_0)} l_0^9}{8} \quad (11)$$

Additionally, when an electric field is applied normal to a film interface, an electrical disjoining pressure is developed because of the Maxwell stress induced at the fluid interface.[18,74,75] This stress can be computed by solving the following Laplace equation between the two electrodes by assuming the film and the bounding medium to be perfect dielectric media with no free charge carriers.

$$\nabla^2 \psi_i = 0 \; (i = 1, 2) \quad (12)$$

where ψ_i is the potential in fluid i. The boundary conditions for the electrostatic problem are defined as

$$\begin{aligned} \psi_1 &= \psi_{low} && \text{at} \quad z = 0 \\ \psi_1 &= \psi_2 && \text{at} \quad z = h(x,y,t) \\ \varepsilon_1 \frac{\partial \psi_1}{\partial z} &= \varepsilon_2 \frac{\partial \psi_2}{\partial z} && \text{at} \quad z = h(x,y,t) \\ \psi_2 &= 0 && \text{at} \quad z = d \end{aligned} \quad (13)$$

By solving the above set of equations analytically for a thin film trapped between two homogeneous electrodes, the derived electrostatic disjoining pressure and the electric field at the film−bounding fluid interface are given by,[3,67] respectively,

$$\phi_{EL} = 0.5\varepsilon_0 \frac{\varepsilon_1}{\varepsilon_2}(\varepsilon_2 - \varepsilon_1) {E_1}^2 \quad (14)$$

and

$$E_1 = \frac{\psi_{low}\varepsilon_2}{\varepsilon_1(d-h) + \varepsilon_2 h} \quad (15)$$

Finally, the overall pressure acting on the thin film considered in this study can be summed as

$$\phi = \phi_{LW} + \phi_{B_L} + \phi_{B_U} + \phi_{EL} \quad (16)$$

Scaling. The scaling of the problem can be realized and derived from a linear stability formulation for the thin film equation.[18,29,74] In this study, we have considered only the case where $\varepsilon_1/\varepsilon_2 (= \varepsilon_p) > 1$. Accordingly, the generalized forms of the time (t^*), length (x^*), and dominant length (λ_c) scales as given by Verma et al.[3] from the linear stability analysis are

$$\begin{aligned} t^* &= \frac{3\mu\gamma {h_0}^3}{[0.5\varepsilon_0\varepsilon_p(\varepsilon_p - 1){\psi_{low}}^2]^2} \\ x^* &= \sqrt{\frac{\gamma {h_0}^3}{0.5\varepsilon_0\varepsilon_p(\varepsilon_p - 1){\psi_{low}}^2}} \end{aligned} \quad (17)$$

$$(\lambda_c)_{EL} = 2\pi\sqrt{\frac{2\gamma\psi_{low}}{\varepsilon_0\varepsilon_p(\varepsilon_p - 1)^2}} {E_1}^{-3/2} \quad (18)$$

Numerical Solution Methodology. The governing equations (eqs 5, 6, and 16) were solved numerically, and a spatiotemporal solution was obtained using a combination of finite difference to resolve the spatial dimensions and an adaptive time step ODE solver for the temporal propagation. More specifically, the discretization of spatial derivatives was carried out using finite differences to reduce the partial differential equation system to a differential algebraic equation (DAE) system in time, which was then solved by employing an adaptive time stepping differential algebraic solver (DASSL).[76] For any specific operating condition, a uniform Cartesian grid with a domain size of 4 times the corresponding critical wavelength (i.e., $L = 4\lambda_c$) was used throughout this work. Periodic

boundary conditions were employed in both the x and y directions. Sensitivity to the grid spacing was checked in the initial numerical simulations, and the results obtained using 90×90 spatial grids were found to be adequate.

To demonstrate the behavior of thin liquid film drainage under an external electric field, a typical thin film system having the properties as shown in Table 1 on a completely wettable substrate has been considered. The Born repulsion force on the lower surface was not involved in simulations because the film was initially stable on the surface as a result of the repulsive van der Waals force on the lower substrate. The bounding fluid was assumed to be inert.

To analyze the thin film drainage behavior, characteristic time and to understand the influence of the liquid viscosity and surface tension, several sets of films with different physical properties were studied. Once the effects of these variations are realized for an electrically homogeneous field, a periodically heterogeneous electrical field is introduced to observe and compare aspects of the characteristic behavior of the drainage time and surface pattern formation. Thereafter, the effects of variations in the periodicity, pitch, and stripe width of the heterogeneity on the film drainage were systematically studied. Finally, the combined chemical and electrical heterogeneity was tested to understand its effect on the film drainage. In all cases, considerable attention was also devoted in recognizing the surface patterns evolved during film drainage.

Table 1. Parameters Used in Simulations

parameter	value
permittivity of free space (ε_0)	8.85×10^{-12} C V^{-1} m^{-1}
dielectric constant of the film (ε_1)	2.5 (−)
dielectric constant of the bounding fluid (ε_2)	1−80 (−)
viscosity (μ)	1 Pa s
interfacial tension (γ)	0.035 N m^{-1}
initial film thickness (h_0)	20−80 nm
effective Hamaker constant (A)	$(-)5 \times 10^{-21}$ J
applied voltage (ψ_{low})	20 V
electrode spacing (d)	100−188 nm

RESULTS AND DISCUSSION

Homogeneous Electric Field. As mentioned earlier in this work, we have focused only on cases with $\varepsilon_1 > \varepsilon_2$, and all the results are discussed by assuming $\varepsilon_p = 2.5$. Figure 3 shows a series of images that represent the morphological evolution of the film−bounding fluid interface formed by the drainage of an initially 20 nm film subjected to a homogeneous electric field ($\psi_{up} = 0$, $\psi_{low} = 20$ V, $E_1 = 90.91$ MV m^{-1}) created by two electrodes having a fixed spacing of 100 nm ($d = d_1 = d_2 = 100$ nm). It demonstrates the rise of liquid columns at random spots, which becomes prominent in time. In the quasi-steady state, these columns wet the upper electrode surface and noticeably do not coalesce even for prolonged exposure. The diameters of these quasi-stable liquid columns are found to be approximately $\lambda_c/2$, and the number density of columns corresponds to the linear theory expectations (16 columns for the $4\lambda_c \times 4\lambda_c$ domain).[3]

With the increase in initial film thickness from 20 to 50 nm, the spatiotemporal evolution of the film becomes quite different (Figure 4). Because of the rapid formation of liquid columns and as the contact line spreads out on the top plate, columns quickly grow in cross section to form elliptical bases with an average column diameter that is larger than $\lambda_c/2$. Over time, nearby liquid columns begin to coalesce more rapidly, leading to structures with larger cross-sectional areas in the final stages.

When the initial film thickness is further increased to 80 nm, the coalescence process of the initially developed liquid columns is extremely fast. As a result of faster intercolumn coalescence,

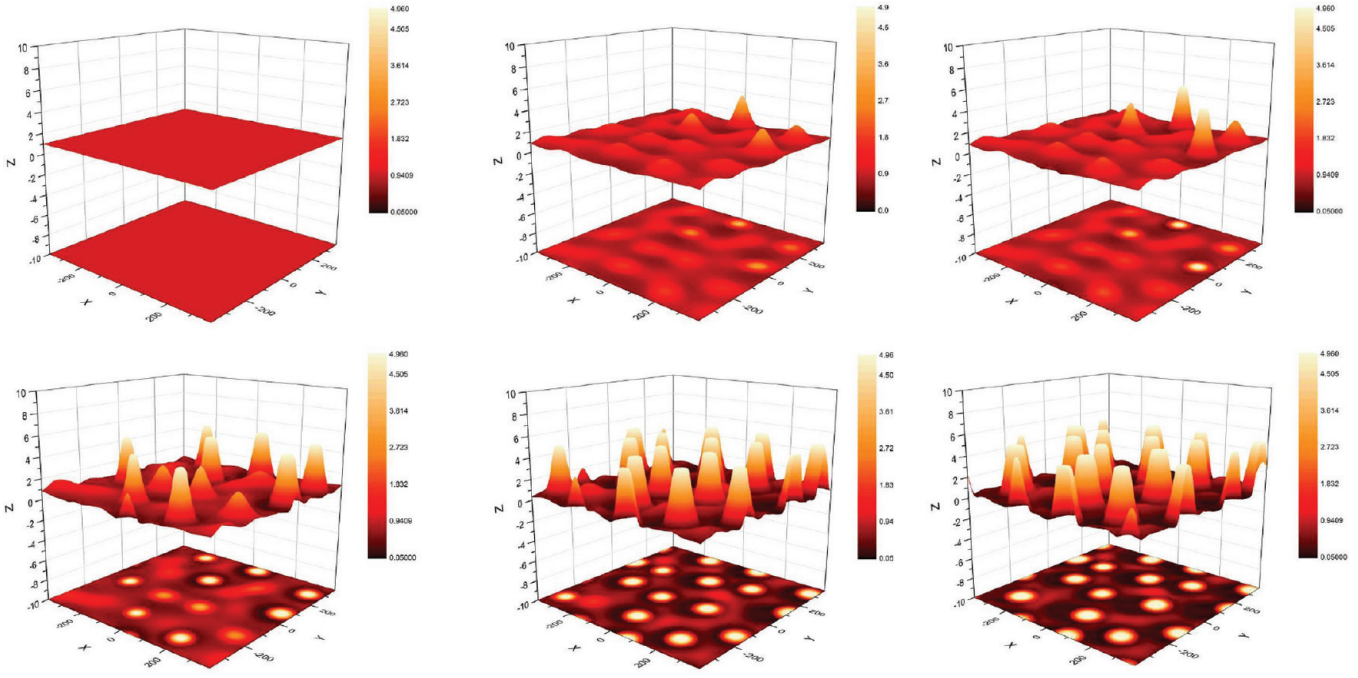

Figure 3. Evolution of a 20 nm film on a $4\lambda_c \times 4\lambda_c$ domain in space and time ($\psi_{low} = 20$ V; initial $E_1 = 90.91$ MV m^{-1}). The nondimensional times for the images are ($T \times 10^{-5}$=) 1, 61.1, 62.1, 66.1, 72.1, and 75.4, respectively.

dx.doi.org/10.1021/la202759j |Langmuir 2011, 27, 12472–12485

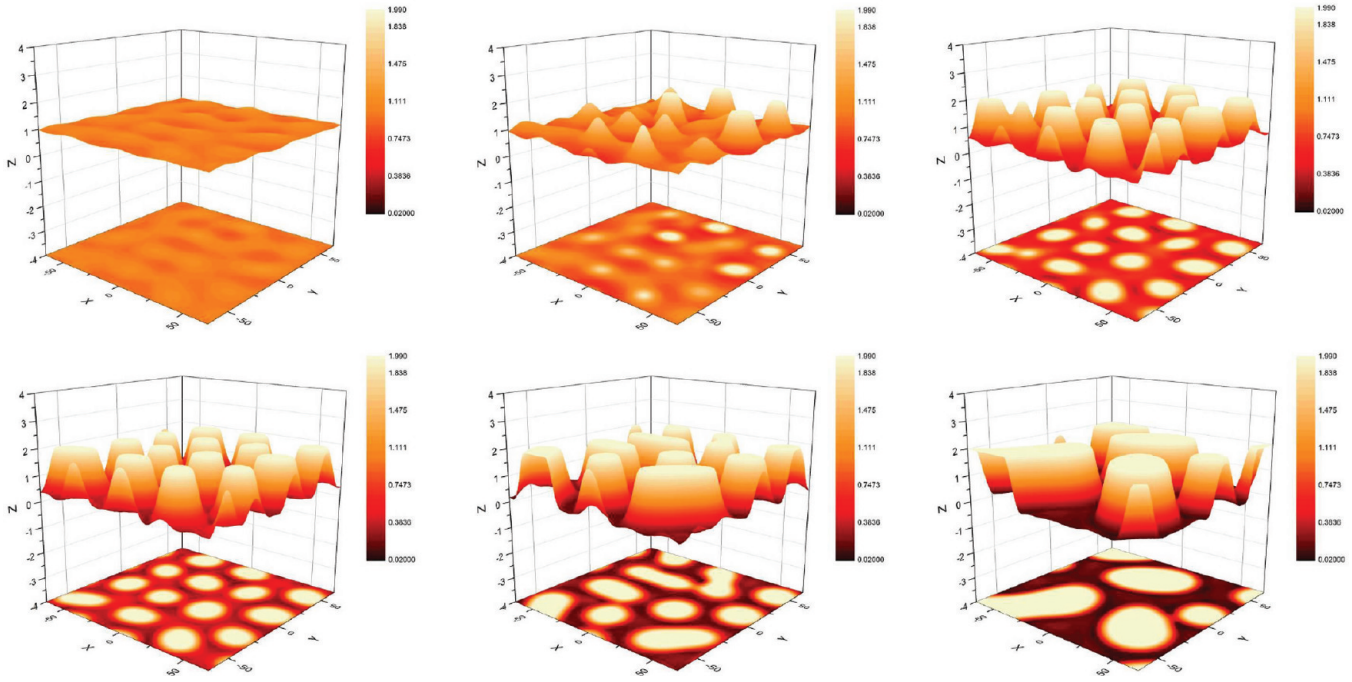

Figure 4. Evolution of a 50 nm film on a $4\lambda_c \times 4\lambda_c$ domain in space and time ($\psi_{low} = 20$ V; initial $E_1 = 114.29$ MV m^{-1}). The nondimensional times for the images are ($T \times 10^{-3}$ =) 5, 6, 7, 8, 11, and 22, respectively.

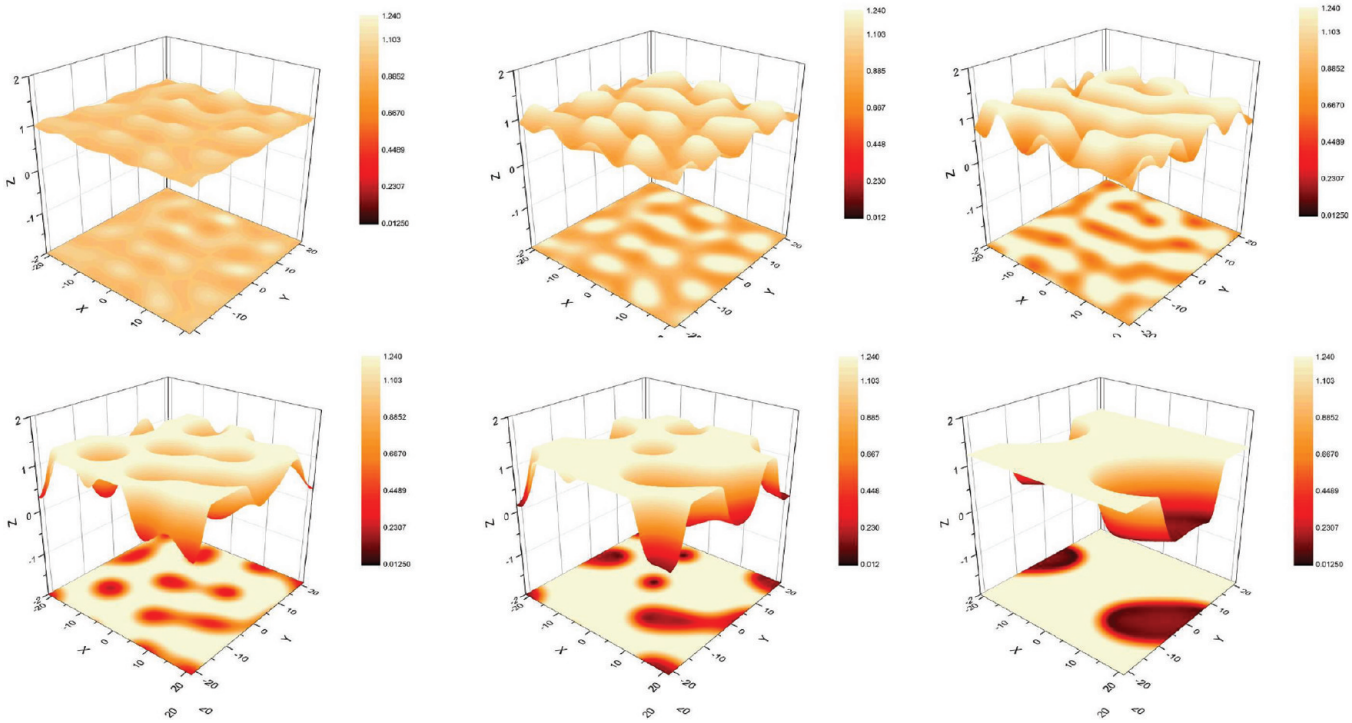

Figure 5. Evolution of an 80 nm film on a $4\lambda_c \times 4\lambda_c$ domain in space and time ($\psi_{low} = 20$ V; initial $E_1 = 153.85$ MV m^{-1}). The nondimensional times for the images are ($T \times 10^{-1}$ =) 5, 6, 8, 16, 42, and 139.1, respectively.

continuous liquid channels are formed, finally resulting in complete phase inversion from the initial liquid-in-air dispersion to an air-in-liquid dispersion[3] (Figure 5).

The drainage time of these thin films has been compared in Figure 6. The maximum (solid line) and minimum film (dashed line) thickness at any given time for any specific film was tracked. The minimum thickness was found by locating the fastest growing hole and the time at which it "touched" the lower substrate. The maximum thickness was followed by identifying the time at which the contact line was approached at the upper

dx.doi.org/10.1021/la202759j |*Langmuir* 2011, 27, 12472–12485

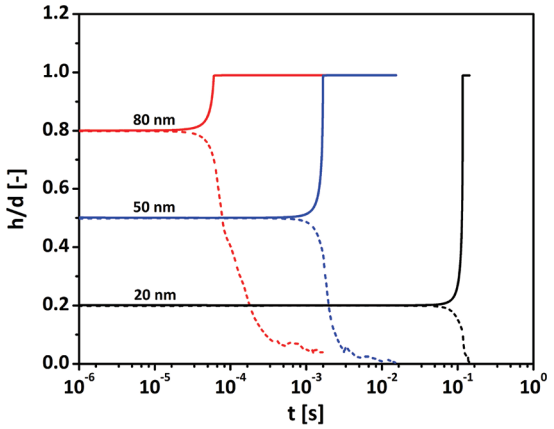

Figure 6. Characteristic drainage behavior comparison for films with different initial thicknesses. Minimum and maximum nondimensional film thicknesses are represented by dashed and solid lines, respectively.

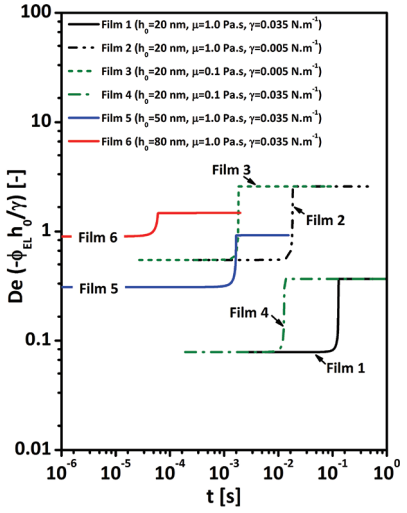

Figure 7. Influence of the electric field strength on films with different viscosities and surface tensions under a homogeneous electric field (ψ_{low} = 20 V).

electrode. The results of different initial film thicknesses indicate that a comparatively thicker film drains more rapidly.

The reason behind this phenomenon is portrayed in Figure 7, where for a comparative analysis of the drainage time the modified Derjaguin's number (De, defined as $-\phi_{EL}h_0/\gamma$) has been plotted against time. This dimensionless number effectively depicts the influence of the maximum electrostatic interaction energy (ϕ_{EL}) due to an external field on thin films having different initial thicknesses (h_0) and surface tensions (γ). Figure 7 shows that comparatively thicker films drain more rapidly as the initial applied electric field is intensified when the ratio of the bounding fluid gap to the thickness of the liquid layer is lower (i.e., when there is a larger volume fraction of a higher dielectric constant fluid in the gap).

Additionally, Figure 7 also provides insight into the comparative drainage behavior of thin films having different surface tension and viscosity. As the viscosity (μ) appears only in the time scaling of the problem (eqs 17 and 18), it can be recognized that it does not affect the morphological evolution of the films but influences the drainage time considerably. As shown in Figure 7, for less viscous films, the applied field will reach its maximum faster and thus will always drain faster for any given operating condition (e.g., film 3 vs film 2 and film 4 vs film 1 in Figure 7). The effect of surface tension can be perceived when films 2 and 3 are compared against films 1 and 4, respectively. Films with reduced surface tension experienced a higher field strength in less time, which leads to faster drainage.

Heterogeneous Electric Field. To compare the drainage pattern with previously discussed homogeneous drainage, the effect of the heterogeneous electric field has been explored. The electric field at the film interface can be varied spatially by changing either the applied electric potential or the electrode spacing. In this study, periodic changes in the electric field are created using spatially varying electrode spacing $d = d(x, y)$, with a constant applied electric potential difference between the upper and lower solid electrodes. Figure 2 demonstrates the schematic of the modeled heterogeneity. By varying the pitch (i.e., the center-to-center distance of adjacent stripes of the same type) (L_p) and stripe width (w), various structures of the upper electrode were achieved for parametric studies. For such geometries, a higher electric field can be realized at the positions with closer electrode spacings (i.e., with $z = d_1$ where $d_1 < d_2$).

Several sets of simulations were carried out for these heterogeneous systems (Table 2). To impose the initial field strength of the homogeneous case (on 20 nm film) as the initial higher field (90.91 MV m^{-1}) and its half strength on the lower field (45.46 MV m^{-1}) periodically, the height variation was selected accordingly (d_1 = 100 nm and d_2 = 188 nm). The first three sets (1−3) in Table 2 help in determining the effect of pitch variation on the drainage behavior. A comparison of sets 1, 6, and 7 provides insights into the estimation of the stripe width variation, and finally, the results in sets 3−5 determine the effect of the initial film thickness for a heterogeneous field.

Influence of the Pitch Variation. Figure 8 shows the evolution of an initial 20 nm film under the influence of a spatially periodic applied electric field with a periodicity of $L_p = 2\lambda_c$ and a width of $w = \lambda_c$. Figure 8a shows a schematic representation of the modeled upper electrode. Figure 8b−g represents the spatiotemporal evolution of the film thickness at the indicated times. The film drains from a small perturbation with a mean initial thickness of h_0 = 20 nm (Figure 8b). Depressions (moats) form on the stripes at a lower applied field, and ridges form on the stripes at a higher applied field (Figure 8c,d). As the ridges develop (Figure 8e), they become unstable and split into a series of circular columns (Figure 8f). The "equilibrium" film morphology can be seen in Figure 8g. A remarkably ordered structure evolves at equilibrium, which essentially consists of parallel rows of circular columns. The columns actually connect the top and bottom electrodes. The rows of liquid columns are found to be uniform in the x direction with an approximate spacing of $2\lambda_c$, which indeed is the periodicity of the upper electrode pattern. In the y direction, the spacing between the consecutive columns is also observed to be uniform with a spacing of approximately λ_c (center-to-center distance). Furthermore, the diameter of each liquid column has a uniform circular cross section with a diameter of close to $\lambda_c/2$, which conforms to the linear theory predictions as observed in the homogeneous field case.

For a reduced pitch value (i.e., an increased number density of stripes forming the structure of the upper electrode as shown in Figure 9a; $L_p = \lambda_c$ and width $w = \lambda_c/2$), the spatiotemporal

Table 2. Parameters Used in the Simulation for Thin Films under a Periodically Heterogeneous Field

		h_0 (nm)	w (λ_c)	L_p (λ_c)
	For Electrical Heterogeneity			
pitch variation	set 1	20	1	2
	set 2	20	0.5	1
	set 3	20	0.25	0.5
film thickness variation	set 4	50	0.25	0.5
	set 5	80	0.25	0.5
stripe width variation	set 6	20	0.5	2
	set 7	20	0.10	2
	For Combined Heterogeneity			
conformational variation ($A = -5 \times 10^{-21}$ J and -5×10^{-19} J)	eclipsed	20	1	2
	staggered	20	1	2
	chemical w/a constant field	20	1	2

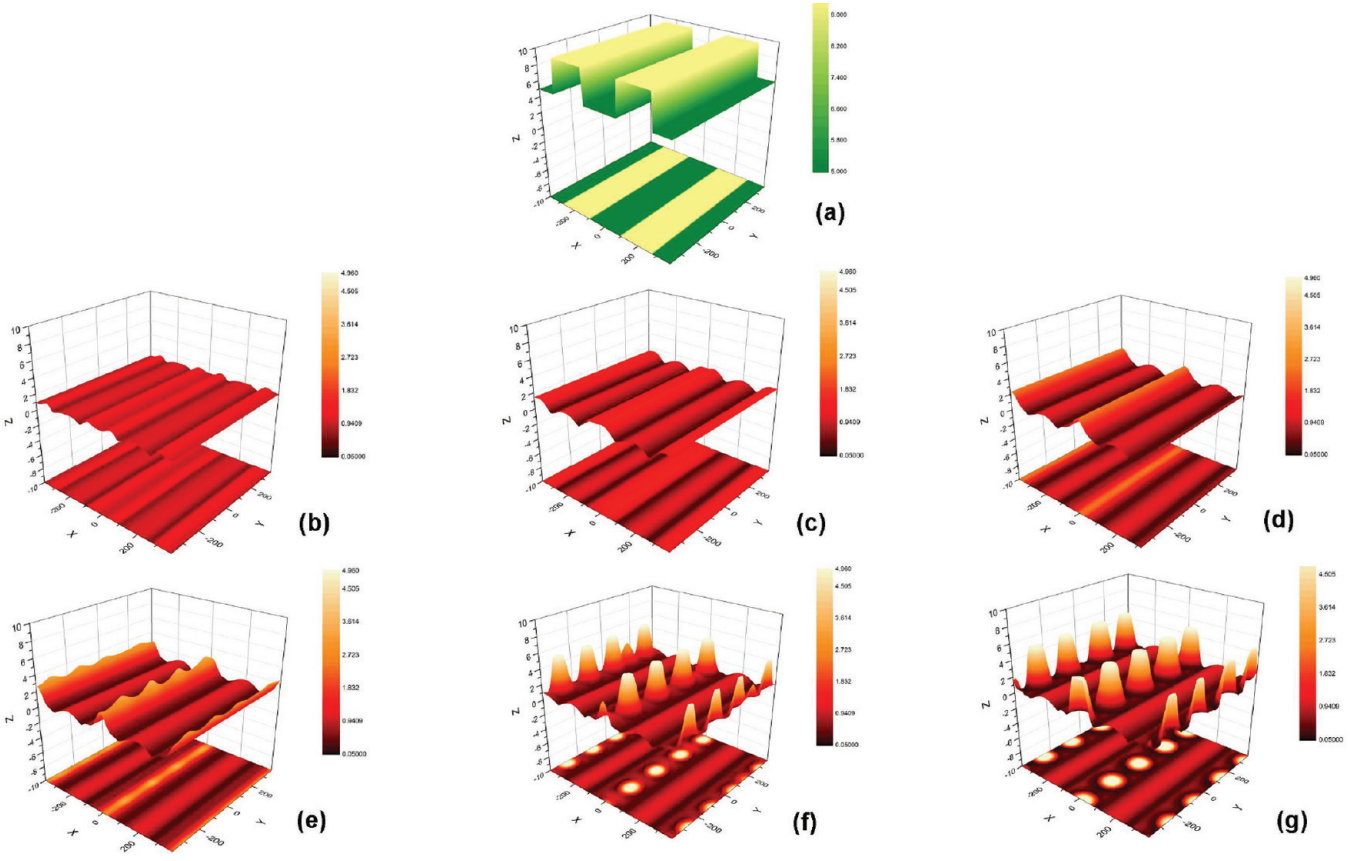

Figure 8. Evolution of a 20 nm film under a periodically heterogeneous electric field ($\psi_{low} = 20$ V, $w = \lambda_c$, and $L_p = 2\lambda_c$). The nondimensional times for the images are ($T \times 10^{-5}$ =) 1, 5, 7, 8, 9, and 14, respectively.

evolution of a 20 nm film draining under the influence of heterogeneously applied electric fields is represented by Figure 9b–g. Similar to the previous discussions, ordered patterns were found where under each protrusion of the upper electrode there was formation of a circular liquid column. Moreover, the rows of liquid columns are found to be uniform in both the x and y directions with a spacing of approximately λ_c. It is noteworthy that in this case the periodicity of the upper electrode pattern was λ_c. As in the previous cases, the diameter of the each circular liquid column was observed to be nearly $\lambda_c/2$.

With further increases in the number density of the stripes ($L_p = \lambda_c/2$ and width $w = \lambda_c/4$, Figure 10a), not every electrode protrusion at the upper electrode could develop the desired liquid columns in the final film morphology as a consequence of the large surface energy requirement for deformation on small scales (Figure 10b). In this case, the developed liquid columns become slightly elliptical in shape as well as nonuniform in nature with an average diameter of less than $\lambda_c/2$.

Figure 11 shows the comparative drainage times of all three aforementioned heterogeneous cases against the homogeneously

dx.doi.org/10.1021/la202759j |*Langmuir* 2011, 27, 12472–12485

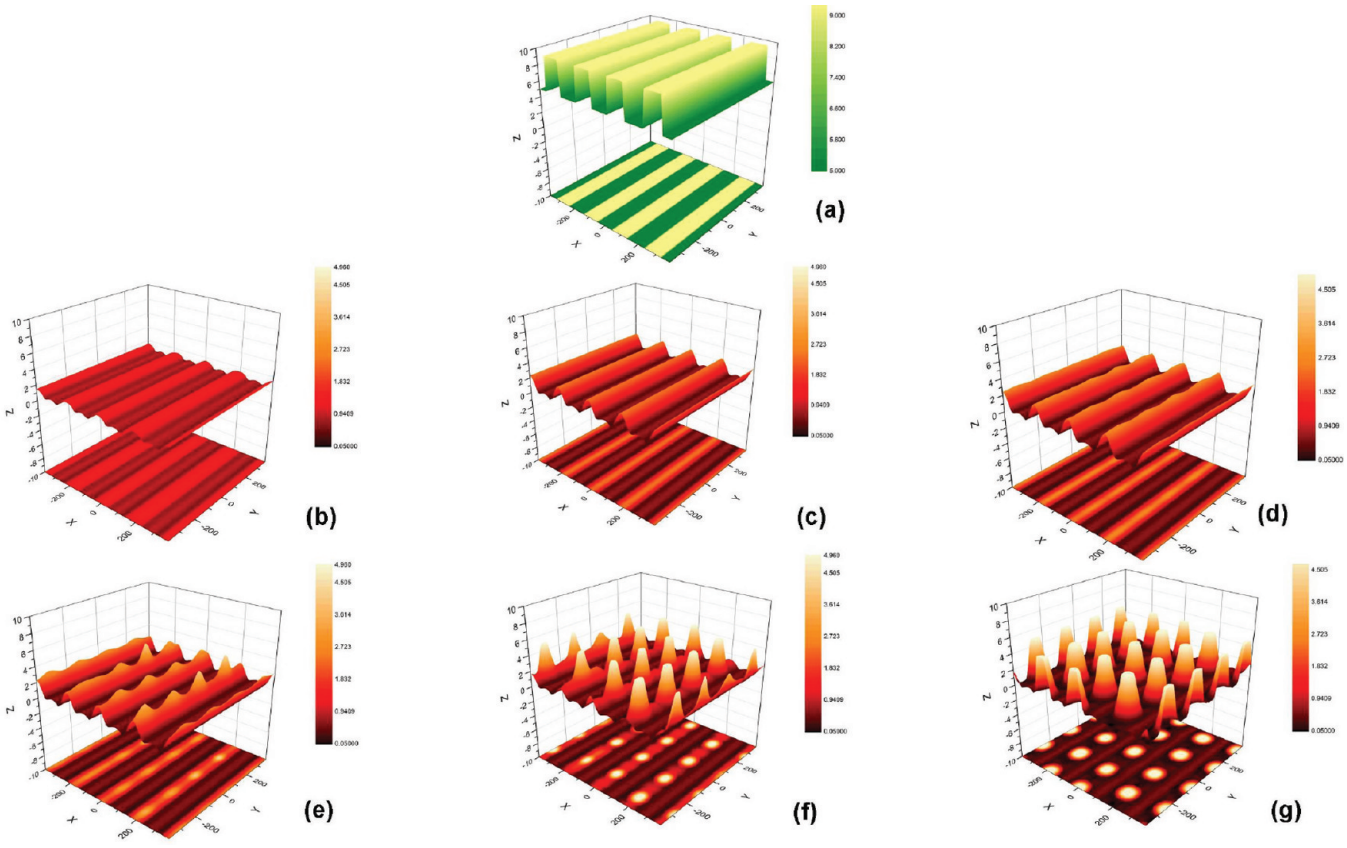

Figure 9. Evolution of a 20 nm film under a periodically heterogeneous electric field (ψ_{low} = 20 V, $w = \lambda_c/2$, and $L_p = \lambda_c$). The nondimensional times for the images are ($T \times 10^{-5}$ =) 1, 5, 7, 8, 9, and 16.7 respectively.

applied electric field. Similar to the homogeneous case, the maximum and minimum film thicknesses (solid and dashed lines, respectively) at any given time for any specific film have been followed. The drainage is not significantly influenced by electrode pattern changes; however, all heterogeneous cases result in faster drainage than for the homogeneously applied field. The frequent spatial alteration of the electric field may result in faster drainage in the initial period, but the time required to reach the quasi-steady or equilibrium state of the surface patterning becomes longer.

Effect of Initial Film Thickness. Similar to the homogeneous field studies, in the case of a heterogeneous field, a faster drainage time was realized for relatively thicker films. However, a significant divergence from the earlier cases in surface patterning has been observed. The quasi-stable morphological evolution of a 50 nm film is shown in Figure 10c when it was exposed to a heterogeneous field with the maximum number density of stripes considered in this study ($L_p = \lambda_c/2$, $w = \lambda_c/4$). It can be observed that contrary to the homogeneous field case, for a 50 nm thin film (Figure 4), phase inversion takes place from the liquid-in-air dispersion to the air-in-liquid dispersion rapidly under the exposure of a periodically heterogeneous field. With further increases in the initial film thickness to 80 nm, very interesting phenomena have been observed. Unlike the homogeneous field case for the 80 nm thin film (Figure 5), in the final stage the film drains only from the sides, leaving a corrugated top surface identical to the upper electrode patterning (Figure 10d). The final-stage morphology can be conceived as a soft imprint of the upper electrode on the film surface.

Influence of Stripe Width. Figure 12 shows the maximum and minimum nondimensional film thickness for an initial 20 nm film under the influence of a different stripe width having a fixed period ($L_p = 2\lambda_c$, $w = \lambda_c$, $0.5\lambda_c$, and $0.1\lambda_c$). Relatively faster drainage was observed in all cases of heterogeneity than for the homogeneous case. When the provided stripe width of the higher electric field is largest among all of the heterogeneous cases, a marginal improvement via faster drainage of the film was observed over the other periodically heterogeneous cases. This case (set 7) also poses an interesting scenario of approaching the limiting case of a completely homogeneous field. The results show that with the introduction of the minimal field heterogeneity the drainage time can be reduced significantly. However, the appearance of contact line at the upper electrode was comparatively faster when the stripe width of a lower field strength was maximized.

Figure 13 represents the spatiotemporal evolution of a 20 nm thin film when exposed to a patterned electric field with constant $L_p = 2\lambda_c$ but $w = 0.5\lambda_c$ (Figure 13a) and $0.1\lambda_c$ (Figure 13d). In both the cases, similar kinds of evolution have been observed. However, with the increasing width of a higher electric field, the accomplishment of a quasi-steady state of the surface pattern requires a longer field exposure. It can be observed that at sufficiently large intermediate time steps very similar kinds of quasi-stable surface patterns were formed in both cases but at different times (Figure 13b,e). This feature is distinctly different from the case where the width of the lower electric field (w) was provided as being equal to the dimension of critical wavelength ($w = w_1 = \lambda_c$, Figure 8). Under prolonged exposure, nearby liquid

dx.doi.org/10.1021/la202759j |*Langmuir* 2011, 27, 12472–12485

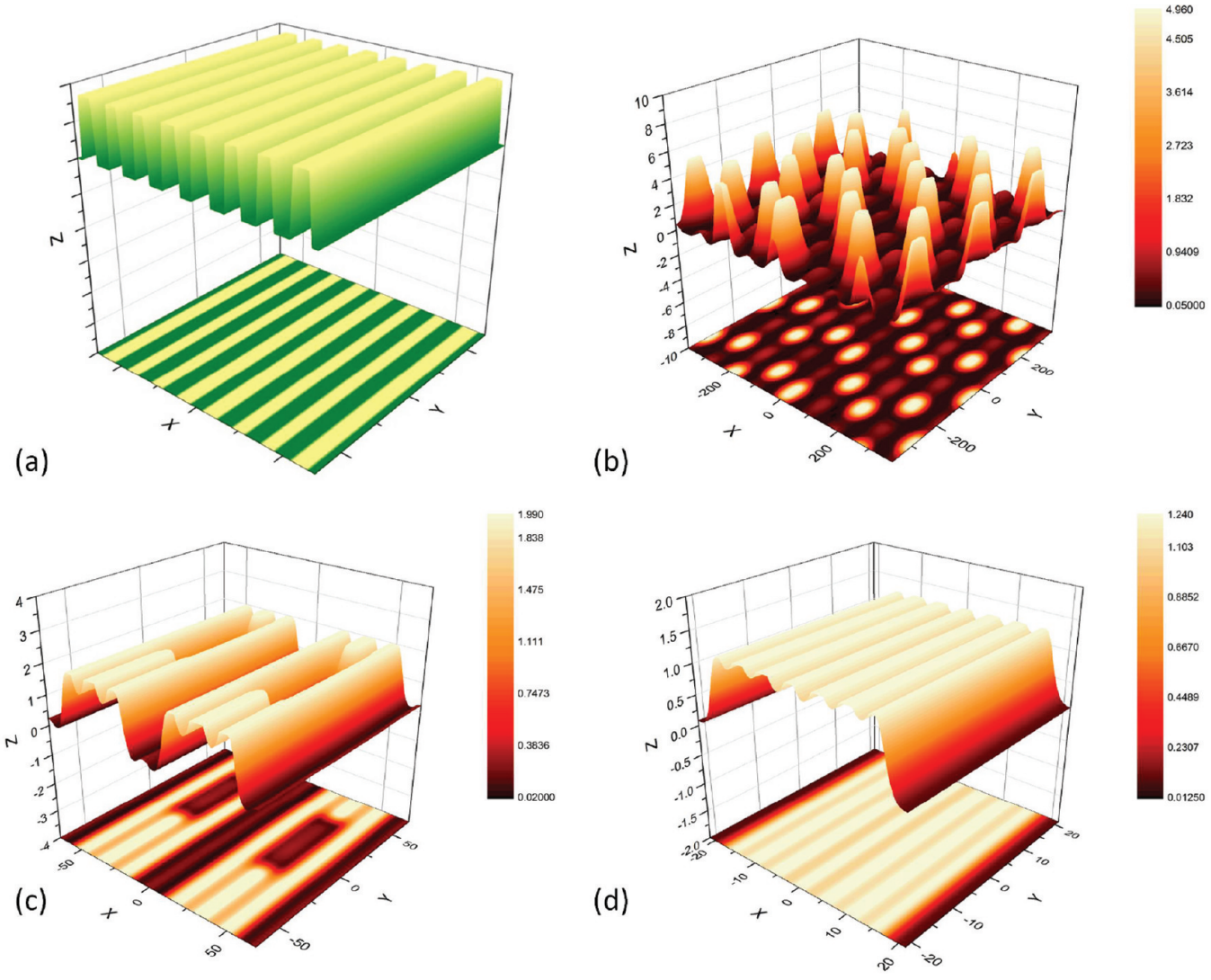

Figure 10. (a) Representation of the modeled upper electrode when $w = \lambda_c/4$ and $L_p = \lambda_c/2$ on a $4\lambda_c \times 4\lambda_c$ domain. Quasi-stable morphologies under such a periodically heterogeneous electric field (ψ_{low} = 20 V) for (b) h_0 = 20 nm at $T = 58.8\times 10^5$, (c) h_0 = 50 nm at $T = 50\times 10^3$, and (d) h_0 = 80 nm at $T = 8.1\times 10^3$.

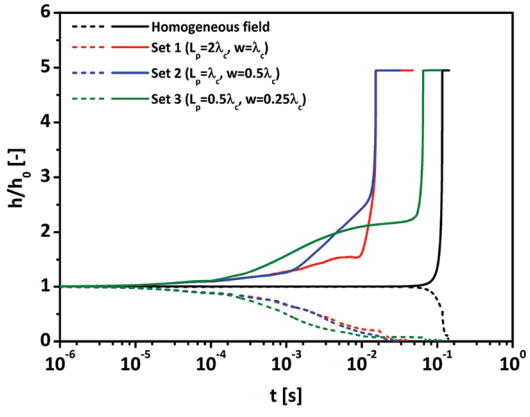

Figure 11. Characteristic drainage behavior under the influence of pitch variation (h_0 = 20 nm and ψ_{low} = 20 V). Minimum and maximum nondimensional film thicknesses are represented by dashed and solid lines, respectively.

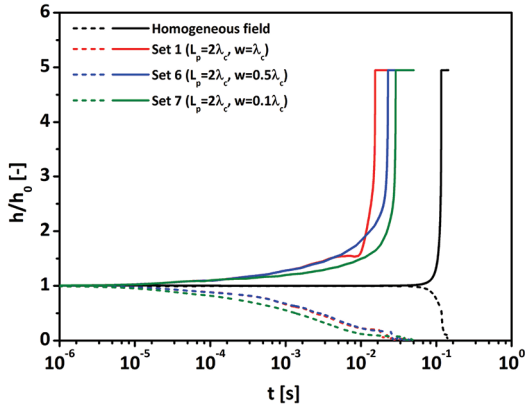

Figure 12. Characteristic drainage behavior under the influence of the stripe width variation (h_0 = 20 nm, ψ_{low} = 20 V). Minimum and maximum nondimensional film thicknesses are represented by dashed and solid lines, respectively.

dx.doi.org/10.1021/la202759j |*Langmuir* 2011, 27, 12472–12485

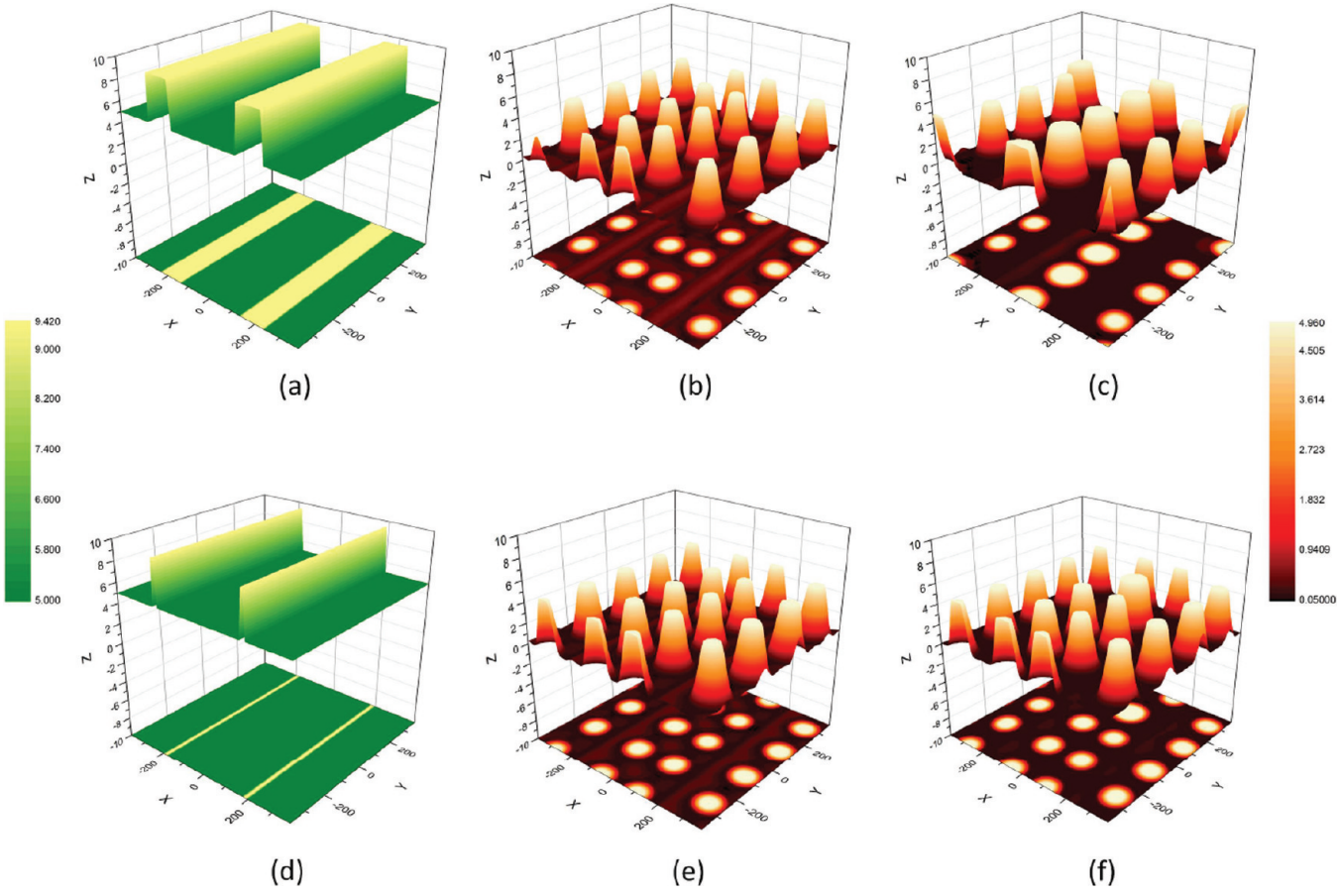

Figure 13. (a) Representation of the modeled upper electrode when $w = 0.5\lambda_c$ and $L_p = 2\lambda_c$ on a $4\lambda_c \times 4\lambda_c$ domain. Evolution of a 20 nm film under such a periodically heterogeneous electric field (ψ_{low} = 20 V) at (b) $T = 2 \times 10^6$ and (c) $T = 5.2 \times 10^6$. (d) Representation of the modeled upper electrode when $w = 0.1\lambda_c$ and $L_p = 2\lambda_c$ on a $4\lambda_c \times 4\lambda_c$ domain. Evolution of a 20 nm film under such a periodically heterogeneous electric field at (e) $T = 4 \times 10^6$ and (f) $T = 34.4 \times 10^6$.

columns in the central region coalesce and form another quasi-stable structure as shown in Figure 13c. As mentioned earlier, for $w = 0.1\lambda_c$, it takes a significantly longer time to reach another quasi-stable stage identical to that in Figure 13c, but the initiation of coalescence is shown in Figure 13f. These results provide strong motivation to understand the utility of precise control over the electric field exposure time. Structured but completely different surface patterns can be achieved at different intermediate stages for any specific case where the stripe width of a higher electric field is larger than the critical wavelength. In addition to faster drainage, these results also indicate that with the introduction of the minimal electric field heterogeneity (Figure 13d), structured surface patterns can be formed, which are not achievable via a homogeneously applied field (Figure 3).

Combined Heterogeneity. Finally, the chemical heterogeneity of the lower substrate has been integrated into this model along with the existing periodic electrical heterogeneity. As mentioned earlier, instead of a dielectric constant mismatch,[61] in this study the chemical heterogeneity has been taken into account by periodic changes in the effective Hamaker constant. The thin film system under the influence of the spatially periodic striping of the applied electric field and effective Hamaker constant at the lower plate is depicted schematically in Figure 14. There can be three distinct scenarios of this combined heterogeneity. When the higher applied electric field

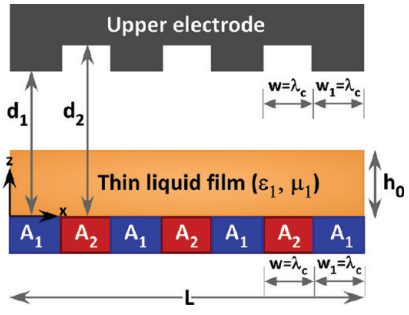

Figure 14. Schematic of the considered combined heterogeneous system. Thin film is resting on a smooth but chemically patterned substrate. The patterned upper electrode (d_1 = 100 nm, d_2 = 188 nm) is used in cases of eclipsed and staggered heterogeneity; however, a flat electrode ($d_1 = d_2$ = 100 nm) is considered for the case of chemical heterogeneity with a constant field. For eclipsed heterogeneity, $A_1 = -5 \times 10^{-19}$ J and $A_2 = -5 \times 10^{-21}$ J; for staggered heterogeneity, $A_1 = -5 \times 10^{-21}$ J and $A_2 = -5 \times 10^{-19}$ J.

(i.e., lower electrode spacing) and larger effective Hamaker constant occur on the same stripes, the pattern will be referred to as the eclipsed combined heterogeneity. If the higher applied electric field and smaller effective Hamaker constant occur on the same stripe, then the pattern will be referred to as the

dx.doi.org/10.1021/la202759j |*Langmuir* 2011, 27, 12472–12485

staggered combined heterogeneity. As discussed in the Introduction, another situation may arise when a system with chemical heterogeneity at the substrate surface is exposed under a homogeneous electric field.

The effects of all of these heterogeneities on the drainage behavior are compared with the cases of isolated electrical heterogeneity (set 1 in Table 2) and a homogeneous field. The parameters taken for the combined heterogeneity studies are listed in Table 2. It can be observed from Figure 15 that the drainage pattern is almost identical in cases of purely electrical-based drainage and eclipsed combined heterogeneity. Complete drainage in cases of combined patterns takes place faster than when only chemical heterogeneity with a homogeneous electric field exists; however, the time difference for complete drainage between two combined patterns is comparable. This phenomenon can be attributed to the large pressure scaling effect due to the long-range electrostatic force over a significantly shorter-ranged LW force. Only chemical heterogeneity with a uniform electric field takes longer time to drain the film but still provides a shorter drainage time than does the homogeneous case. It also produces distinctly different surface patterns at the equilibrium stage (Figure 16). Figure 16 also shows that the surface patterns in the equilibrium stage resulting from the eclipsed combined heterogeneity and purely electrical heterogeneity are similar, having perceptible ridges separating two developed liquid columns in the y direction; however, in the case of staggered heterogeneity, the separation between two liquid columns is flattened and complete drainage is experienced from those positions. To preserve the overall liquid volume, the diameter of the liquid columns in the middle is larger than in the two earlier

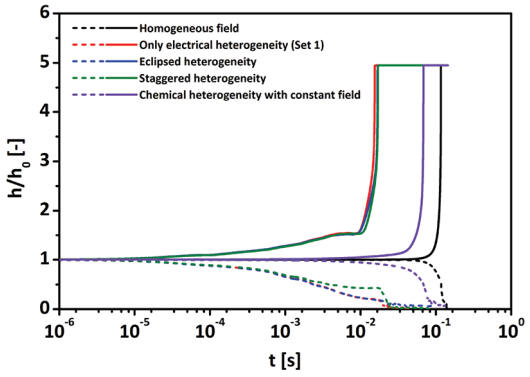

Figure 15. Characteristic drainage behavior comparison under the influence of combined heterogeneity (h_0 = 20 nm, ψ_{low} = 20 V). Minimum and maximum nondimensional film thicknesses are represented by dashed and solid lines, respectively.

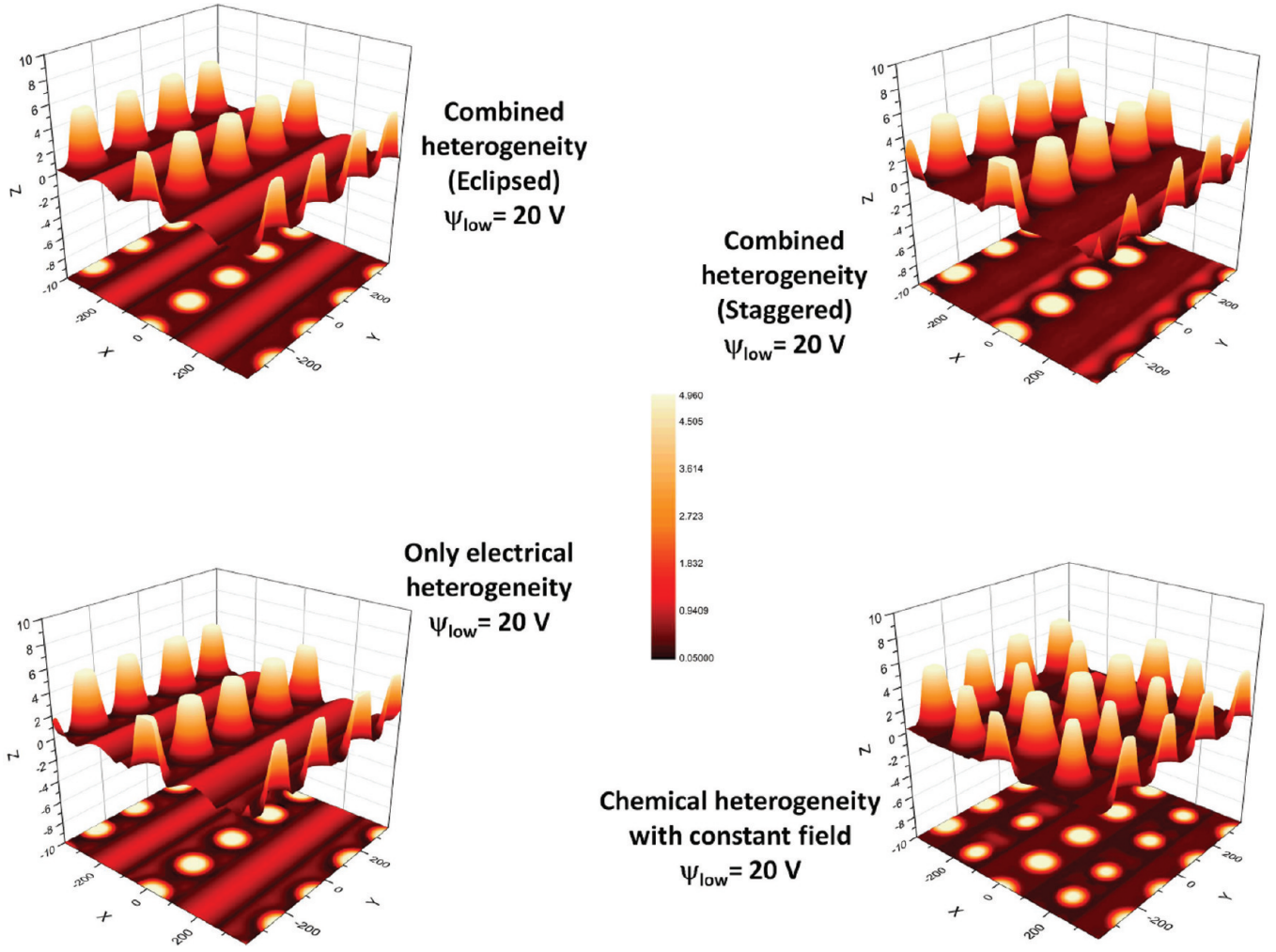

Figure 16. Summary of quasi-steady states under different types of heterogeneity on a $4\lambda_c \times 4\lambda_c$ domain (ψ_{low} = 20 V).

dx.doi.org/10.1021/la202759j |*Langmuir* 2011, 27, 12472–12485

cases. Under purely chemical heterogeneity with a homogeneous electric field, the equilibrium surface morphology is visibly different from that in all other heterogeneous cases.

CONCLUDING REMARKS

The drainage behavior of a thin liquid film under the influence of an external electric field has been presented. It is demonstrated that a significantly faster drainage of the thin film can be achieved by lowering the viscosity and surface tension in the presence of a homogeneously applied electric field. Even faster drainage can be achieved by introducing a periodic electric field heterogeneity. Relatively thicker films drain faster as a result of experiencing a higher force field in a shorter time. In all cases, the electrical breakdown of the thin liquid film occurs by the formation of submicrometer-scale structures. Electrical heterogeneity results in ordered submicrometer-scale surface patterning, which closely depends on the ratio of the electrode spacing to the initial film thickness. The pitch and stripe width of the periodic electrical heterogeneity determine the equilibrium morphology of the fluid−fluid interface and the film drainage time. When the width of the higher field area is larger than the corresponding critical length scale, then novel surface patterns can be achieved at intermediate quasi-steady stages, which over time ripen and cause adjacent columns to coalesce. Because of the substantial difference in the pressure scale, the effect of chemical heterogeneity is dominated by the electrical heterogeneity. However, the results show that the presence of chemical heterogeneity under a homogeneous electric field leads to slightly faster film drainage when compared to the drainage based solely on the homogeneous electric field. Even though the combination of chemical and electrical heterogeneity does not contribute significantly to the drainage time, it is certainly an attractive option for creating interesting surface patterns while synthesizing materials with novel nano- and microscale morphologies.

These results are significant from the perspective of several technological applications (e.g., electroporation, faster de-emulsification, novel material synthesis, etc.). Moreover, this developed model with combined heterogeneity can effectively serve as the basis for emulating the electrical perturbation of thin liquid films in many practical scenarios. Along with several other parameters, the design of an efficient electrostatic coalescer requires a fundamental understanding of the thin film drainage, the effects of electrode design, and the electric field configuration. To achieve rapid de-emulsification, this work opens up the exciting possibilities of harnessing the applied field heterogeneity and optimizing its configuration according to the emulsion properties. Therefore, this theoretical study is presented with the hope that it shall encourage experimental studies on emulsion film rupture using heterogeneous electric fields.

AUTHOR INFORMATION

Corresponding Author

*E-mail: subir.b@ualberta.ca.

ACKNOWLEDGMENT

We acknowledge financial support from the Natural Sciences and Engineering Research Council (NSERC), Canada, the Alberta Water Research Institute (AWRI), Kemira, Outotec, and Suncor Energy.

REFERENCES

(1) Danov, K. D.; Valkovska, D. S.; Ivanov, I. B. *J. Colloid Interface Sci.* **1999**, *211*, 291–303.
(2) Yan, X. H.; Liu, G. J.; Dickey, M.; Willson, C. G. *Polymer* **2004**, *45*, 8469–8474.
(3) Verma, R.; Sharma, A.; Kargupta, K.; Bhaumik, J. *Langmuir* **2005**, *21*, 3710–3721.
(4) Mukherjee, R.; Gonuguntla, M.; Sharma, A. *J. Nanosci. Nanotechnol.* **2007**, *7*, 2069–2075.
(5) Eow, J. S.; Ghadiri, M.; Sharif, A. O.; Williams, T. J. *Chem. Eng. J.* **2001**, *84*, 173–192.
(6) Stubenrauch, C.; von Klitzing, R. *J. Phys.: Condens. Matter* **2003**, *15*, R1197–R1232.
(7) Sjöblom, J.; Urdahl, O.; Høiland, H.; Christy, A.; Johansen, E. In *Surfactants and Macromolecules: Self-Assembly at Interfaces and in Bulk*; Lindman, B., Rosenholm, J., Stenius, P., Eds.; Progress in Colloid and Polymer Science; Springer: Berlin, 1990; Vol. 82, pp 131−139.
(8) Khristov, K.; Taylor, S. D.; Czarnecki, J.; Masliyah, J. *Colloids Surf., A* **2000**, *174*, 183–196.
(9) Ruckenstein, E.; Sharma, A. *J. Colloid Interface Sci.* **1987**, *119*, 1–13.
(10) Anklam, M. R.; Saville, D. A.; Prud'homme, R. K. *Langmuir* **1999**, *15*, 7299–7307.
(11) Anklam, M. R.; Saville, D. A.; Prud'homme, R. K. *Colloid Polym. Sci.* **1999**, *277*, 957–964.
(12) Favazza, C.; Kalyanaraman, R.; Sureshkumar, R. *J. Appl. Phys.* **2007**, *102*, 104308.
(13) Trice, J.; Favazza, C.; Thomas, D.; Garcia, H.; Kalyanaraman, R.; Sureshkumar, R. *Phys. Rev. Lett.* **2008**, *101*, 017802.
(14) Krishna, H.; Shirato, N.; Yadavali, S.; Sachan, R.; Strader, J.; Kalyanaraman, R. *ACS Nano* **2011**, *5*, 470–476.
(15) Ghatak, A.; Khanna, R.; Sharma, A. *J. Colloid Interface Sci.* **1999**, *212*, 483–494.
(16) Bandyopadhyay, D.; Sharma, A. *J. Phys. Chem. C* **2010**, *114*, 2237–2247.
(17) Wu, N.; Russel, W. B. *Appl. Phys. Lett.* **2005**, *86*, 241912.
(18) Schaffer, E.; Thurn-Albrecht, T.; Russell, T. P.; Steiner, U. *Nature* **2000**, *403*, 874–877.
(19) Voicu, N.; Harkema, S.; Steiner, U. *Adv. Funct. Mater.* **2006**, *16*, 926–934.
(20) Voicu, N. E.; Saifullah, M. S. M.; Subramanian, K. R. V.; Welland, M. E.; Steiner, U. *Soft Matter* **2007**, *3*, 554–557.
(21) Craster, R.; Matar, O. *Rev. Mod. Phys.* **2009**, *81*, 1131–1198.
(22) Mukherjee, R.; Das, S.; Das, A.; Sharma, S. K.; Raychaudhuri, A. K.; Sharma, A. *ACS Nano* **2010**, *4*, 3709–3724.
(23) Lenz, R. D.; Kumar, S. *Phys. Fluids* **2007**, *19*, 102103.
(24) Lenz, R. D.; Kumar, S. *J. Fluid Mech.* **2007**, *571*, 33–57.
(25) Kalpathy, S. K.; Francis, L. F.; Kumar, S. *J. Colloid Interface Sci.* **2010**, *348*, 271–279.
(26) Oron, A.; Davis, S.; Bankoff, S. *Rev. Mod. Phys.* **1997**, *69*, 931–980.
(27) Wu, N.; Russel, W. B. *Nano Today* **2009**, *4*, 180–192.
(28) Sharma, A.; Khanna, R. *J. Chem. Phys.* **1999**, *110*, 4929.
(29) Schaffer, E.; Thurn-Albrecht, T.; Russell, T.; Steiner, U. *Europhys. Lett.* **2001**, *53*, 518–524.
(30) Harkema, S.; Steiner, U. *Adv. Funct. Mater.* **2005**, *15*, 2016–2020.
(31) Favazza, C.; Kalyanaraman, R.; Sureshkumar, R. *Nanotechnology* **2006**, *17*, 4229–4234.
(32) Das, A. L.; Mukherjee, R.; Katiyer, V.; Kulkarni, M.; Ghatak, A.; Sharma, A. *Adv. Mater.* **2007**, *19*, 1943–1946.
(33) Gonuguntla, M.; Sharma, A.; Mukherjee, R.; Subramanian, S. A. *Langmuir* **2006**, *22*, 7066–7071.
(34) Mukherjee, R.; Pangule, R.; Sharma, A.; Tomar, G. *Adv. Funct. Mater.* **2007**, *17*, 2356–2364.
(35) Mukherjee, R.; Pangule, R. C.; Sharma, A.; Banerjee, I. *J. Chem. Phys.* **2007**, *127*, 064703.
(36) Mukherjee, R.; Bandyopadhyay, D.; Sharma, A. *Soft Matter* **2008**, *4*, 2086–2097.

(37) Mukherjee, R.; Sharma, A.; Patil, G.; Faruqui, D.; Pattader, P. S. G. *Bull. Mater. Sci.* **2008**, *31*, 249–261.
(38) Pattader, P. S. G.; Banerjee, I.; Sharma, A.; Bandyopadhyay, D. *Adv. Funct. Mater.* **2011**, *21*, 324–335.
(39) Verma, A.; Sharma, A.; Kulkarni, G. *Small* **2011**, *7*, 758–765.
(40) Lee, S. H.; Kim, P.; Jeong, H. E.; Suh, K. Y. *J. Micromech. Microeng.* **2006**, *16*, 2292–2297.
(41) Wu, N.; Pease, I.; Leonard, F.; Russel, W. B. *Adv. Funct. Mater.* **2006**, *16*, 1992–1999.
(42) Xiang, H. Q.; Lin, Y.; Russell, T. P. *Macromolecules* **2004**, *37*, 5358–5363.
(43) Morariu, M. D.; Voicu, N. E.; Schaffer, E.; Lin, Z. Q.; Russell, T. P.; Steiner, U. *Nat. Mater.* **2003**, *2*, 48–52.
(44) Verma, R.; Sharma, A.; Banerjee, I.; Kargupta, K. *J. Colloid Interface Sci.* **2006**, *296*, 220–232.
(45) Dickey, M.; Gupta, S.; Leach, K.; Collister, E.; Willson, C.; Russell, T. *Langmuir* **2006**, *22*, 4315–4318.
(46) Lyutakov, O.; Huettel, I.; Prajzler, V.; Jerabek, V.; Jancarek, A.; Hnatowicz, V.; Svorcik, V. *J. Polym. Sci., Part B: Polym. Phys.* **2009**, *47*, 1131–1135.
(47) Wu, N.; Kavousanakis, M. E.; Russel, W. B. *Phys. Rev. E* **2010**, *81*, 026306.
(48) Bae, J.; Glogowski, E.; Gupta, S.; Chen, W.; Emrick, T.; Russell, T. P. *Macromolecules* **2008**, *41*, 2722–2726.
(49) Dickey, M.; Collister, E.; Raines, A.; Tsiartas, P.; Holcombe, T.; Sreenivasan, S.; Bonnecaze, R.; Willson, C. *Chem. Mater.* **2006**, *18*, 2043–2049.
(50) Dickey, M. D.; Raines, A.; Collister, E.; Bonnecaze, R. T.; Sreenivasan, S. V.; Willson, C. G. *J. Mater. Sci.* **2008**, *43*, 117–122.
(51) Lu, W.; Kim, D. *Appl. Phys. Lett.* **2006**, *88*, 153116.
(52) Pease, L. F.,; Russel, W. B. *J. Chem. Phys.* **2006**, *125*, 184716.
(53) Wu, N.; Russel, W. B. *Ind. Eng. Chem. Res.* **2006**, *45*, 5455–5465.
(54) Yeoh, H. K.; Xu, Q.; Basaran, O. A. *Phys. Fluids* **2007**, *19*, 114111.
(55) Sarkar, J.; Sharma, A.; Shenoy, V. B. *Phys. Rev. E* **2008**, *77*, 031604.
(56) Li, B.; Li, Y.; Xu, G.-K.; Feng, X.-Q. *J. Phys.: Condens. Matter* **2009**, *21*, 445006.
(57) Roberts, S. A.; Kumar, S. *Phys. Fluids* **2010**, *22*, 122102.
(58) Bandyopadhyay, D.; Sharma, A.; Thiele, U.; Reddy, P. D. S. *Langmuir* **2009**, *25*, 9108–9118.
(59) Gambhire, P.; Thaokar, R. M. *Phys. Fluids* **2010**, *22*, 064103.
(60) Reddy, P. D. S.; Bandyopadhyay, D.; Sharma, A. *J. Phys. Chem. C* **2010**, *114*, 21020–21028.
(61) Srivastava, S.; Reddy, P. D. S.; Wang, C.; Bandyopadhyay, D.; Sharma, A. *J. Chem. Phys.* **2010**, *132*, 174703.
(62) Craster, R. V.; Matar, O. K. *Phys. Fluids* **2005**, *17*, 032104.
(63) Taylor, S. D.; Czarnecki, J.; Masliyah, J. *J. Colloid Interface Sci.* **2002**, *252*, 149–160.
(64) Mostowfi, F.; Czarnecki, J.; Masliyah, J.; Bhattacharjee, S. *J. Colloid Interface Sci.* **2008**, *317*, 593–603.
(65) Mostowfi, F.; Khristov, K.; Czarnecki, J.; Masliyah, J.; Bhattacharjee, S. *Appl. Phys. Lett.* **2007**, *90*, 184102.
(66) Panchev, N.; Khristov, K.; Czarnecki, J.; Exerowa, D.; Bhattacharjee, S.; Masliyah, J. *Colloids Surf., A* **2008**, *315*, 74–78.
(67) Crawford, D. G.; Koch, C. R.; Bhattacharjee, S. *J. Comput. Theor. Nanosci.* **2008**, *5*, 2060–2066.
(68) Kralchevsky, P. A.; Nagayama, K. *Particles at Fluid Interfaces and Membranes*; Elsevier: Amsterdam, 2001.
(69) Lenz, R. D.; Kumar, S. *J. Colloid Interface Sci.* **2007**, *316*, 660–670.
(70) Ruckenstein, E.; Jain, R. *J. Chem. Soc., Faraday Trans. 2* **1974**, *70*, 132–147.
(71) Williams, M.; Davis, S. *J. Colloid Interface Sci.* **1982**, *90*, 220–228.
(72) Sharma, A.; Jameel, A. *J. Colloid Interface Sci.* **1993**, *161*, 190–208.
(73) Mitlin, V. *J. Colloid Interface Sci.* **1993**, *156*, 491–497.
(74) Shankar, V.; Sharma, A. *J. Colloid Interface Sci.* **2004**, *274*, 294–308.
(75) Masliyah, J. H.; Bhattacharjee, S. *Electrokinetic and Colloid Transport Phenomena*; Wiley-Interscience: Hoboken, NJ, 2005.
(76) Brenan, K.; Petzold, L. *SIAM J. Numer. Anal.* **1989**, *26*, 976–996.